

Measurement of the Dispersion of $\chi^{(3)}$ of SiO₂ and SiN Across the THz and Far-Infrared Frequency Bands

Binbin Zhou, Mattias Rasmussen, Soheil Zibod, Siqi Yan, Narwan Kabir Noori, Oliver Nagy, Yunhong Ding, Simon Jappe Lange, Ksenia Dolgaleva, Robert W. Boyd, and Peter Uhd Jepsen*

Terahertz (THz) radiation sources based on two-color femtosecond plasmas in air are becoming a mature technology for coherent spectroscopy and strong-field physics across the extended THz range to several tens of THz. The field-resolved detection of such THz transients relies on the third-order nonlinearity of the detection medium. Here, a comparative measurement is demonstrated with air-biased coherent detection (ABCD) and solid-state biased detection (SSBCD) as a novel method to measure the dispersion of the magnitude and phase of the relevant third-order nonlinearity $\chi^{(3)}(2\omega \pm \Omega; \omega, \omega, \pm\Omega)$ for fused silica (SiO₂) and silicon nitride (SiN). Based on the development of the ultrabroadband SSBCD device with a detection bandwidth exceeding 30 THz, $\chi^{(3)}$ measurements are obtained across the 1–28 THz frequency range, hence covering the THz and far-infrared. It is shown that the vibrational modes in SiO₂ and SiN in the THz range lead to strong resonant enhancement and dispersion of the nonlinearity. The SSBCD devices operate down to nanojoule (nJ) probe energy, and their is demonstrated by measuring the dielectric function of the Lorentzian line profile of transverse-optical (TO) phonon mode at 9 THz in single-crystal gallium arsenide (GaAs) and observing the weak phonon combination bands near the TO phonon.

the detection of THz-frequency electromagnetic waves is the so-called ABCD (Air Biased Coherent Detection) technique,^[1,2] often used in combination with THz-wave generation in two-color femtosecond air plasma.^[3–5] This combination is referred to as THz air photonics since the media for generation and detection can be as simple as the air in the laboratory, although a pure nitrogen (N₂) atmosphere is beneficial from a spectroscopic point of view due to strong absorption and dispersion arising from the dense band of rotational transitions in the water molecules in ambient air. THz air photonics is a versatile technology for quantitative THz time-domain spectroscopy (THz-TDS) across a very broad spectral window spanning the 1–30 THz range, both in static^[6,7] and time-resolved^[8,9] configurations.

Recently, a complementary solid-state biased detection (SSBCD) scheme was developed for THz waveform detection.^[10,11] Both ABCD and SSBCD rely on the third-order nonlinearity

1. Introduction

Applications relying on radiation in the terahertz (THz) frequency range depend naturally on the efficient generation and detection of THz waves. One of the prominent methods for

of the gaseous or solid-state detection medium for generation of the second-harmonic signal of a probe laser pulse that forms the detection signal. Hence, measurements with ABCD and SSBCD of the same THz signal can be used for quantitative

B. Zhou, M. Rasmussen, O. Nagy, Y. Ding, S. J. Lange, P. U. Jepsen
Department of Electrical and Photonics Engineering
Technical University of Denmark
Kongens Lyngby DK-2800, Denmark
E-mail: puje@dtu.dk

S. Zibod, K. Dolgaleva, R. W. Boyd
School of Electrical Engineering and Computer Science
University of Ottawa
Ottawa, Ontario ON K1N 6N5, Canada

S. Yan
School of Optical and Electronic Information
Huazhong University of Science and Technology
Wuhan 430079, China

N. K. Noori
Photonic Inc. Vancouver
Vancouver, British Columbia BC V3B 6B4, Canada

R. W. Boyd
Department of Physics
University of Ottawa
Ottawa, Ontario ON K1A 9A7, Canada

 The ORCID identification number(s) for the author(s) of this article can be found under <https://doi.org/10.1002/lpor.202301321>

© 2024 The Author(s). Laser & Photonics Reviews published by Wiley-VCH GmbH. This is an open access article under the terms of the [Creative Commons Attribution-NonCommercial-NoDerivs](https://creativecommons.org/licenses/by-nc-nd/4.0/) License, which permits use and distribution in any medium, provided the original work is properly cited, the use is non-commercial and no modifications or adaptations are made.

DOI: 10.1002/lpor.202301321

measurement of the nonlinearity behind the detection principle. This is conceptually similar to most types of spectroscopy, where light from the same light source interacts with a sample, and the modification of the transmitted or reflected spectrum of the light is analyzed to yield the optical properties of the sample.

To date, the reported SSBCD can only support THz frequency detection up to 10 THz, in part limited by the duration of the applied femtosecond probe pulses. Developing an SSBCD detector with a bandwidth comparable to the ABCD would potentially provide a unique platform for nonlinearity characterization of the solid-state detection medium across the entire THz spectrum. Meanwhile, there has been a keen interest in exploring THz frequency nonlinearities. Most studies have focused either on the low-frequency THz-induced Kerr effects in nonlinear media probed as birefringence in the optical frequency range, where the measured nonlinear refractive index is on the same order of magnitude as in all-optical cases;^[12–14] or on self-induced Kerr effects where only low-frequency THz pulses are involved.^[15–17] In the latter case, notably, $\chi^{(3)}$ coefficients orders of magnitude larger than those at near-infrared or visible wavelengths have been found in the relatively low THz frequency range. In those THz nonlinearity studies, crystal-based (e.g., lithium niobate) high-energy THz sources are commonly employed, restricting the valid THz frequency range from low to approximately 2.5 THz. Despite being very intriguing, the nonlinearity across the broader, higher-frequency THz band remains largely unexplored due to the lack of effective measurement techniques. For instance, it has been numerically predicted that the extraordinarily high THz $\chi^{(3)}$ in the low THz frequencies originated from the material lattice vibrational resonances at the high-frequency THz/MIR range.^[12] However, this is yet to be verified by experimental investigations.

Here, based on the SSBCD THz detector with significantly improved high-frequency performance and bandwidth, we demonstrate a method comprised of a direct comparison of the detected THz transient and its spectrum with ABCD and SSBCD, respectively, which allows us to extract the spectrum of the third-order nonlinearity that drives THz-frequency field-induced second harmonic (TFISH) generation, $\chi^{(3)}(2\omega \pm \Omega; \omega, \omega, \pm\Omega)$, in amorphous SiO₂ and SiN in the range from 1 to >28 THz. We resolve the dispersion of the vibrationally enhanced nonlinearity due to the relation with the linear dielectric response of the materials. To complement the experimental characterization, we develop a first-principles analytical model for the nonlinearity based on an anharmonic oscillator and find almost quantitative agreement of the measured and calculated magnitudes of the nonlinearities.

The method presented here for nonlinear spectroscopy relies on our developed ultrabroadband SSBCD devices. We present detailed descriptions of the devices and show that they are indeed also versatile detectors for linear THz time-domain spectroscopy (THz-TDS) with an ultra-broadband measurement of the near-perfect Lorentzian line shape of the transverse-optical (TO) phonon in gallium arsenide (GaAs) and its much weaker phonon combination bands below and above the TO phonon frequency.

2. Theoretical Background

Coherent detection of THz fields can be performed with the general method of field-induced second-harmonic generation.

Here, the third-order nonlinearity of a medium is the relevant physical interaction term. In general, the third-order nonlinearity $\chi^{(3)}$ of the susceptibility is responsible for a plethora of nonlinear effects, including the self-induced Kerr effect ($\chi^{(3)}(\omega; \omega, -\omega, \omega)$), exploited for instance in Kerr-lens mode-locking in the near-infrared^[18] and also observed in the THz frequency range with absolute strength orders of magnitude larger than at shorter wavelength,^[12–14] THz field-induced Kerr effect ($\chi^{(3)}(\omega; \omega, \Omega, -\Omega)$) in the optical range,^[15–17] third-harmonic generation ($\chi^{(3)}(3\omega; \omega, \omega, \omega)$), and field-induced second-harmonic generation. The electric field generated by the nonlinear polarization oscillating at $2\omega \pm \Omega$ is $E_{2\omega \pm \Omega} \propto P_{2\omega \pm \Omega}^{(3)} = \epsilon_0 \chi^{(3)}(2\omega \pm \Omega; \omega, \omega, \Omega) E_\omega^2 E_\Omega$. In the context of THz air photonics, the component at $\omega + \omega - \Omega$ will dominate due to better phase matching in a Gaussian focus.^[19] For convenience, in the following, we will refer to this specific component of the third-order susceptibility in short form as $\chi^{(3)}$. For $\Omega = 0$ the term is responsible for electric-field-induced second-harmonic generation (ESHG). It has been applied for measurements of $\chi^{(3)}(\omega)$ of gases^[20] relative to reference gas (He) based on ab initio calculations.^[21] Cook et al. introduced TFISH ($\Omega > 0$) as a measurement technique probing the correlation between hyperpolarizability and dipole moment fluctuations at equilibrium in liquids.^[22] The TFISH technique was applied by Dai et al. as an efficient way to detect THz waveforms using $\chi^{(3)}$ of air or a nitrogen atmosphere.^[1] They showed that under special conditions (high intensity of the probe field at ω) the intensity of the 2ω signal contains a component proportional to the THz field strength. Karpowicz et al. then extended the TFISH technique with a static bias field, thereby enabling easy coherent detection of the THz field by the technique now known as air-biased coherent detection (ABCD).^[2] The oscillating field at 2ω now has a contribution induced by the THz field and a contribution from the static field. If the bias field is modulated symmetrically as $\pm E_{\text{bias}}$ the interference between these contributions leads to an intensity of the generated signal at 2ω ,

$$I_{2\omega \pm \Omega} \propto (\chi^{(3)} I_\omega)^2 [E_{\text{THz}}^2 \pm 2E_{\text{bias}} E_{\text{THz}} + E_{\text{bias}}^2] \quad (1)$$

Using lock-in detection at the bias modulation frequency, the interference term is isolated, and the detected signal is proportional to the field strength of the THz signal.

2.1. Determination of TFISH $\chi^{(3)}$ of Solid-State Materials

The nonlinear susceptibility $\chi^{(3)}$ of nitrogen (N₂) can be assumed to be virtually dispersion-free across the THz range and the phase-matching between THz frequencies and the probe frequencies is much better than in solid-state materials. Hence ABCD of ultrashort field transients with a broad spectral content across the THz range is a versatile detection technique that offers high-fidelity measurement of the THz waveform only limited by the duration and bandwidth of the probe field, I_ω . In practice, using 30–40 fs probe pulses, detection bandwidths exceeding 30 THz are routinely achieved.

The ABCD technique's limitation is that the probe beam's intensity must be high to generate a detectable signal at 2ω due to the low density and thus low absolute value of $\chi^{(3)}$ of gases. Typically, the probe pulse energy is in the range of 100 μJ , focused to an intensity slightly below the ionization threshold of the gas.

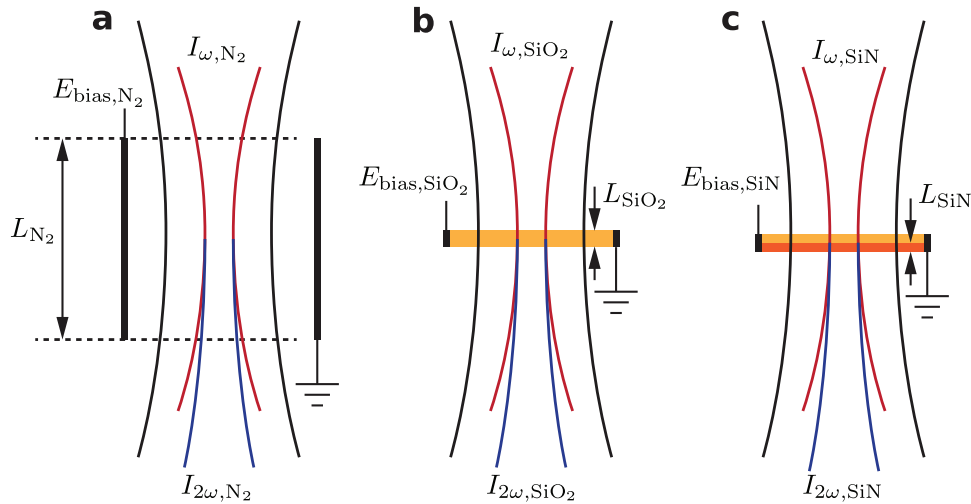


Figure 1. Detection geometry for a) ABCD with N_2 gas as the nonlinear medium, b) SSBCD with SiO_2 as nonlinear medium, and c) SSBCD with SiN embedded in SiO_2 as the nonlinear medium.

Tomasino et al. devised a method to greatly reduce the required intensity of the probe beam by using fused silica (amorphous silicon dioxide, SiO_2) as the nonlinear medium instead of air,^[10] in a solid-state analog to the ABCD, coined SSBCD. The orders-of-magnitude higher nonlinear susceptibility of fused silica lowered the required energy of the probe pulse to the range of 100 nJ, thus enabling femtosecond laser systems with higher repetition rate^[23] and lower pulse energy. The devices were fabricated with gold electrodes separated by narrow slits filled with SiO_2 ^[10] or silicon nitride (SiN).^[11] The narrow-slit geometry further increases the detection efficiency by broadband enhancement of the THz field, especially at lower frequencies.

The detection of THz radiation by either ABCD or SSBCD with lock-in techniques is sensitive to the modulated component of the TFISH signal intensity

$$I_{2\omega} \propto (\chi^{(3)} I_{\omega})^2 E_{\text{bias}} E_{\text{THz}} L^2 \quad (2)$$

where L is the effective distance over which the interaction between the fields take place (see [Supporting Information](#) for a short discussion of the L^2 dependence). For free-space (ABCD) detection, the distance can be defined as the overlap between Rayleigh lengths of the focused probe beam and THz beam (estimated to 2.0 mm in our experiments). For the SSBCD geometry, a combination of the thickness of the dielectric medium, the phase matching length, and the geometric extent of the bias field from the electrodes will determine the effective interaction length L . **Figure 1** illustrates the detection geometries encountered here (ABCD, SSBCD in SiO_2 and SiN).

The ratio between the TFISH signal $I_{2\omega}(\Omega)$ when detected in a solid, such as SiO_2 , and air, respectively, can be used to extract the

complex-valued $\chi^{(3)}(\Omega)_{\text{sol}}$ for the solid, assuming that the same incident THz field strength is used in two consecutive measurements with the two techniques,

$$\chi_{SiO_2}^{(3)}(\Omega) = \chi_{N_2}^{(3)} \frac{L_{N_2}}{L_{SiO_2}} \cdot \frac{I_{\omega,N_2}}{I_{\omega,SiO_2}} \sqrt{\frac{I_{2\omega,SiO_2}(\Omega)}{I_{2\omega,N_2}(\Omega)} \cdot \frac{E_{\text{bias},N_2}}{E_{\text{bias},SiO_2}} \cdot \frac{1}{t_{SiO_2}(\Omega)}} \quad (3)$$

here I_{ω,SiO_2} , I_{ω,N_2} are the optical probe intensities, E_{bias,SiO_2} , E_{bias,N_2} are the modulated bias fields, and L_{SiO_2} , L_{N_2} are the interaction lengths between the probe and the THz field, all in the respective SSBCD and ABCD geometries. The transmission factor $t_{SiO_2}(\Omega)$ accounts for frequency-dependent absorption in SiO_2 , reflection losses, and field enhancement in the gaps between the bias electrodes ($t(\Omega)$ is calculated for the SiO_2 and SiN devices in the [Supporting Information](#)).

The ratio $I_{2\omega,SiO_2}/I_{2\omega,N_2}$ is the complex-valued ratio of the spectra of the THz transients recorded by SSBCD and ABCD, respectively. Hence, it is possible to determine both the magnitude and phase of $\chi^{(3)}(\Omega)$ with this method.

For the specific situation of TFISH detection with our SiN device, one has to consider that the active SiN layer is buried under a 0.5- μm SiO_2 layer, as shown in **Figure 1c**. In this case, we need to consider that the TFISH signal is partly generated in the cap SiO_2 layer, and partly in the SiN layer. Given that the nonlinearity of SiO_2 is already determined by Equation (3), the third-order nonlinearity of the SiN layer can then be extracted (see [Supporting Information](#) for details) according to

$$\chi_{SiN}^{(3)}(\Omega) = \frac{1}{L_{SiN}} \sqrt{\frac{I_{2\omega,SiN}(\Omega)}{I_{2\omega,N_2}(\Omega)} \cdot \left(\frac{I_{\omega,N_2}}{I_{\omega,SiN}}\right)^2 \cdot \frac{E_{\text{bias},N_2}}{E_{\text{bias},SiN}} \cdot \frac{1}{t_{SiO_2}(\Omega)t_{SiN}(\Omega)} \left(\chi_{N_2}^{(3)} L_{N_2}\right)^2 - \frac{1}{t_{SiN}(\Omega)} \left(\chi_{SiO_2}^{(3)} L_{SiO_2}\right)^2} \quad (4)$$

Mizrahi and Shelton^[20] used ESHG to measure the third-order nonlinearity $\chi^{(3)}(2\omega; \omega, \omega, 0)$ of N_2 relative to that of helium (He). The value of the relevant third-order nonlinearity of He can be deduced from the ab initio calculations by Sitz and Yaris.^[21] As shown in the [Supporting Information](#), these results lead to the value $\chi_{N_2}^{(3)} = 1.686 \times 10^{-25} \text{ m}^2\text{V}^{-2}$ that we will use in Equations (3) and (4). It is reasonable to assume that THz-frequency values of the nonlinear susceptibility of N_2 gas will be very close to this value, given that there are no vibrational or rotational resonances in the N_2 molecule across the THz band. On the other hand, the strong dispersion of the linear refractive index (and thus of $\chi^{(1)}$) of the solid is expected to lead to a frequency dependence of its nonlinear susceptibility, $\chi^{(3)}(2\omega \pm \Omega; \omega, \omega, \pm\Omega)$.^[12]

2.2. Theoretical Estimate of $\chi^{(3)}(2\omega \pm \Omega; \omega, \omega, \pm\Omega)$

The frequency dependence of the third-order nonlinearity of a vibrational mode in a solid can be calculated from first principles, based on the anharmonic oscillator model,^[24]

$$\ddot{x} + 2\gamma\dot{x} + \Omega_0^2x + ax^2 + bx^3 = \alpha E(t) \quad (5)$$

where x is the ion displacement from the equilibrium position, γ is damping factor, Ω_0 is the vibrational resonance frequency of the nonlinear medium, $E(t)$ is the applied field and a and b are the second- and third-order nonlinear coefficients, respectively.

If the driving field $E(t)$ consists of a THz-frequency component $E_{\text{THz}}e^{-i\Omega t}$ and an optical frequency component $E_{\text{opt}}e^{-i\omega t}$, the anharmonic oscillator equation can be solved by perturbation theory. As derived in detail in the [Supporting Information](#), such analysis leads to expressions of the third-order nonlinearity due to self-action (THz Kerr effect), $\chi^{(3)}(\Omega; \Omega, -\Omega, \Omega)$, and the term responsible for TFISH generation, $\chi^{(3)}(2\omega \pm \Omega; \omega, \omega, \pm\Omega)$. If the model now contains three individual resonances (indicated by the index k) that are not coupled to each other, the total third-order nonlinearities will be

$$\chi^{(3)}(\Omega; \Omega, -\Omega, \Omega) = \sum_{k=1}^3 \frac{1}{(\Omega_{0,k}^2 - \Omega^2 - 2i\gamma_k\Omega)^3 (\Omega_{0,k}^2 - \Omega^2 + 2i\gamma_k\Omega)} \left[\frac{qN\alpha^3}{3} 2a_k^2 \frac{(3\Omega_{0,k}^2 - 8\Omega^2 - 8i\gamma_k\Omega)}{\Omega_{0,k}^2 (\Omega_{0,k}^2 - 4\Omega^2 - 4i\gamma_k\Omega)} - \frac{3(n_{0,k}^2 - 1)^2}{32N\hbar\pi^2} \frac{\Omega_{0,k}^{11}}{(\Omega_{0,k}^2 - \omega^2 - 2i\gamma_k\omega)^2} \right] \quad (6)$$

$$\chi^{(3)}(2\omega + \Omega; \omega, \omega, \Omega) = \sum_{k=1}^3 \left[\frac{qN\alpha^3}{3} \frac{2a_k^2}{(\Omega_{0,k}^2 - \Omega^2 - 2i\gamma_k\Omega)} \frac{9}{16\omega^8} + \frac{3(n_{0,k}^2 - 1)^2}{32N\hbar\pi^2} \frac{\Omega_{0,k}^{11}}{(\Omega_{0,k}^2 - \Omega^2 - 2i\gamma_k\omega)^2} \frac{1}{4\omega^6 (\Omega_{0,k}^2 - \Omega^2 - 2i\gamma_k\Omega)} \right] \quad (7)$$

$$\chi_k^{(3)}(2\omega - \Omega; \omega, \omega, -\Omega) = \chi_k^{(3)}(2\omega + \Omega; \omega, \omega, \Omega)^* \quad (8)$$

The magnitude and phase of the third-order susceptibilities for THz self-action and TFISH, respectively, are plotted in a semi-logarithmic fashion in [Figure 2a,b](#), respectively, with the three resonance frequencies $\Omega_{0,k}/2\pi = 16.0, 24.0, 37.2$ THz. The damping rates are set equal to $\gamma_k = 5 \times 10^{12} \text{ rads}^{-1}$ ($k = 1, 2, 3$).

As can be seen, for TFISH, the value at low frequency is scaled down by a factor proportional to Ω_0^8/ω^8 . The reason is that the dominant term at low frequency is the term related to the cascaded process (first term) in both the THz self-action process and the TFISH process. For TFISH, four resonance factors disappear compared to THz self-action. Thus, the factor of $(1/\Omega_0^2)^4$ is replaced by $(1/\omega^2)^4$. However, the dominant term for THz self-action and TFISH at the resonance frequency is the direct term corresponding to b . For TFISH, three resonance factors disappear compared to THz self-action. Thus the factor of $(1/\Omega_0^2)^3$ is replaced by $(1/\omega^2)^3$. However, there is another factor of $(1/Q)^3$, where Q is the resonance quality factor calculated as $Q = \Omega_0/\gamma$, due to the three missing enhancement factors at the resonance frequency. The resonances related to two-photon absorption in the THz self-action spectrum near half of each resonance frequency are not replicated in the TFISH spectrum. Hence, there is no simple relation (such as a scaling law) between the self-action and the TFISH nonlinearity, although both originate from the same nonlinear oscillator model.

3. THz-TDS with Air Photonics: Experimental Setup and Spectroscopic Methods

A typical experimental setup for THz time-domain spectroscopy (THz-TDS) using femtosecond two-color air plasma as the source and ABCD or SSBCD as detection is shown in [Figure 3](#). The spectrometer is driven by a femtosecond amplifier with output in the millijoule (mJ) range with a typical center wavelength of 800 nm (Ti:sapphire system) and pulse duration of 35–100 fs. The THz pulse energy is greatly enhanced by using a longer wavelength

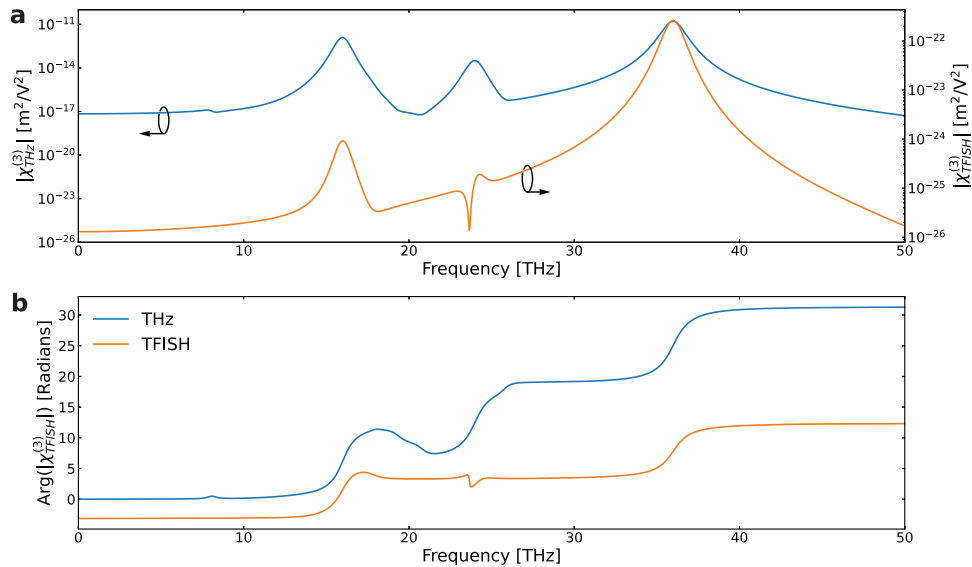


Figure 2. Theoretical third-order nonlinearities of an uncoupled, anharmonic oscillator system with independent resonances at frequencies of 16.0, 24.0, and 37.2 THz. a) Magnitudes and b) phases of the self-action (THz) $\chi^{(3)}$ (Equation (6), blue curves) and TFISH $\chi^{(3)}$ (Equation (7), orange curves).

to drive the air plasma,^[25,26] so we employ an optical parametric amplifier (OPA) that generates pump wavelengths in the 1.1–2.4 μm range. The laser beam is split into two parts for the generation and detection of the THz pulses, respectively. Part of the pump energy is frequency-doubled in a second-harmonic generation (SHG) crystal (BBO), and the polarization of the 2ω beam is rotated by 90 degrees to be aligned with the polarization of the fundamental ω beam by a dual-wavelength wave plate (DWP). The two colors $\omega + 2\omega$ are focused to an intensity sufficient for ionization of the nitrogen atmosphere, forming the plasma region for THz generation. With a few mJ pump energy and a focusing distance 30 cm, the plasma filament is typically 1–3 cm long and visible by its fluorescence. The THz beam is collimated by standard reflective optics in the form of off-axis paraboloidal

mirrors. For spectroscopy, a $f - 2f - 2f - 2f - f$ with an intermediate focal plane is used. A reflection geometry can be realized by inserting a beam splitter and a mirror to pick up the fraction of the THz beam reflected from the sample, as shown in Figure 3. The probe beam is focused in the detection focal plane together with the THz beam, and the TFISH signal centered at 2ω is detected by an avalanche photodiode (APD)^[27] or a photomultiplier tube (PMT). An electric field modulates the TFISH signal from a high-voltage supply (HV), and the modulated signal is detected by lock-in techniques while scanning the delay of the probe pulse.

A spectroscopic measurement is performed by recording a THz pulse in a reference condition, $E_{\text{ref}}(t)$, and a THz pulse in a sample condition, $E_{\text{sam}}(t)$. For a transmission measurement, the reference condition can be to remove the sample from the

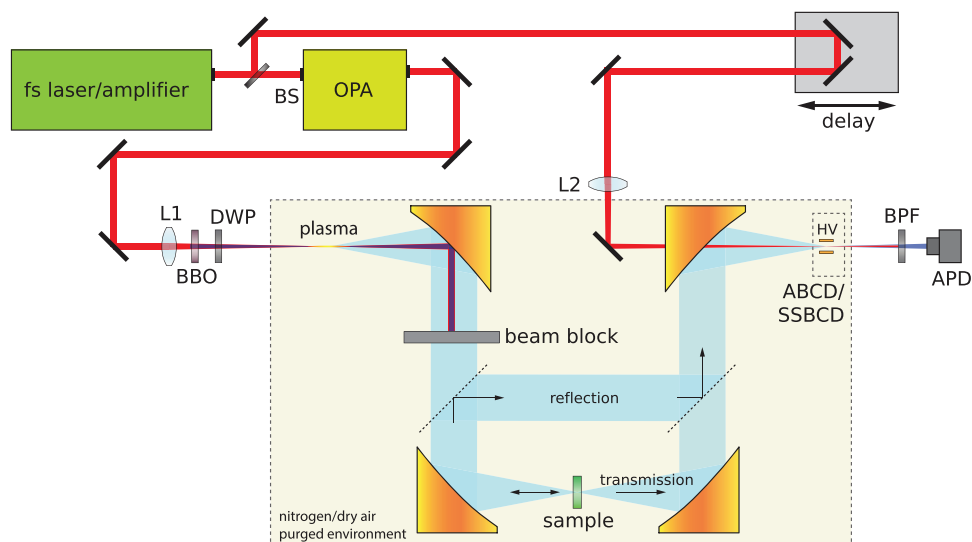


Figure 3. Schematics of a generic THz air photonics setup with two-color air plasma generation and ABCD/SSBCD detection components.

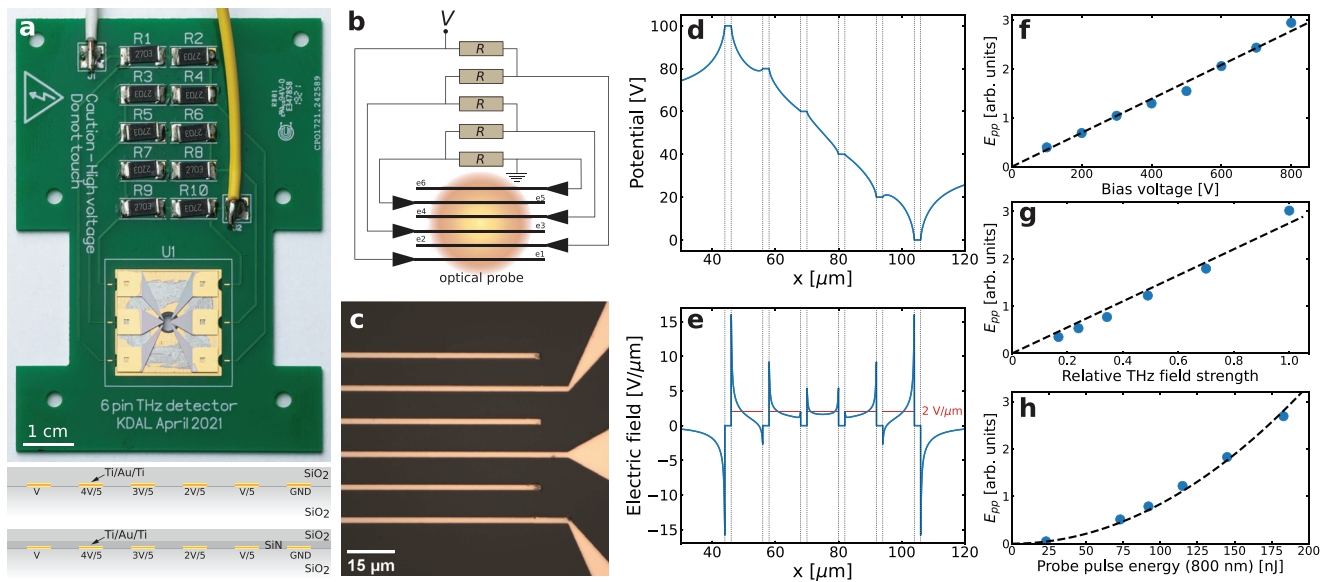


Figure 4. a) Photograph of the complete SSBCD device for ultra-broadband THz waveform detection and cross-section diagram of the electrode region on the chip for the SiO₂ (top) and SiN (bottom) device. b) Voltage divider circuit and electrode arrangement. c) Microscope image of electrode area. d) Simulated electrostatic potential in the plane of the electrodes. e) In-plane bias electric field in the electrode region. f) Bias dependence, g) THz field strength dependence, and h) Optical probe pulse energy dependence of the detector signal.

beam path, or in the case of a measurement of a thin film on a substrate, move the sample to a position where the beam is transmitted through the substrate alone. In reflection geometry, a reference condition can be a reflection from a known material, typically a smooth metallic film.

The mathematical framework for analysis of THz spectroscopic measurements is based on Fresnel reflection and transmission coefficients and propagation of plane waves in a medium with a complex-valued index of refraction. The techniques for THz-TDS are reviewed in many overview articles, e.g., [28]. The starting point of the analysis is the Fourier transforms of the sample and reference signals, $E_{\text{ref}}(\Omega)$ and $E_{\text{sam}}(\Omega)$ with correctly unwrapped phases.^[29]

4. Solid-State Biased Coherent Detection Device

In a solid-state biased coherent detector with a single sub- μm slit design, the relatively low THz frequencies experience significant field enhancement and can therefore be effectively detected. This design was previously used for detecting THz frequencies up to 10 THz (at the -30dB relative intensity level).^[10,11] For THz frequencies above 10 THz, the field enhancement effect from the slit is rather limited and mostly localized to the edge area, and the small throughput flux (for both optical and THz waves) from the single narrow slit may greatly limit the TFISH signal generation and thus detection of high THz frequency components. To facilitate efficient detection of high-frequency THz waves, we implemented a THz-SSBCD design as shown in Figure 4.

We utilize a large active detection area consisting of an electrode array with gaps filled by SiO₂ or SiN. A complete detector, mounted on a printed circuit board, is shown in Figure 4a. Each of the six electrodes is biased with a linearly decreasing potential spanning from the applied external bias to 0 V by a simple

chain of resistors ($R = 540\text{ k}\Omega$, split over two resistors in series), as shown in Figure 4b. A microscope image of the electrode structure is shown in Figure 4c. In this manner, the electrostatic potential between the electrodes is distributed as shown in Figure 4d (finite element simulation with 100 V external bias, see further details in the Supporting Information), leading to a distribution of the bias electric field as shown in Figure 4e.

Our SSBCD device is fabricated on top of a 0.5-mm fused silica substrate. The six-electrode finger structure (Ti/Au/Ti, 20/200/20 nm, length 1 mm, width 2 μm , gap spacing 10 μm) was fabricated by standard UV lithography together with gold fan-out structures for connection of the electrodes to the external circuit. Two different dielectric thin-film deposition processes were applied. For the SiO₂-based detector, a 1- μm SiO₂ film was deposited on top of the electrode finger structures, and for the SiN-based detector, a 0.5- μm SiN film was deposited on the electrode structure and capped by an extra 0.5- μm SiO₂ layer. The total active area of the detectors is then 1 mm by 50 μm , with its width comparable to the diameter (FWHM) of the optical probe beam focus (approximately 40 μm) and thus facilitates optimal TFISH generation in the active area. Compared to a narrow slit detector,^[10,11] THz field enhancement effect in our detector implementation is insignificant, with some enhancement near the electrodes (see Supporting Information). However, the enlarged active detecting area utilizes the full overlapping area between the optical probe and THz focus spot and enhances the overall TFISH signal generation. Detectors with a single wide slit (e.g., 50 μm) can have the same large detecting area, but the highest applicable bias voltage is lower due to the larger penetration of the bias field lines into the air region above the dielectric (see Supporting Information). A thicker dielectric layer can, in principle, be deposited to allow for a higher bias voltage, with the drawback that high-frequency THz waves will be strongly attenuated due to absorption. The ba-

sic functionality of the detector in terms of its linear response to bias voltage and THz field strength, as well as the quadratic response to the intensity of the probe beam, is as expected from earlier work,^[10,11] and is shown in Figure 4f–h. See the [Supporting Information](#) for details on this characterization of our devices. In line with the expected higher absolute value of $\chi^{(3)}$ of SiN compared to SiO₂ under the same conditions of optical probe energy and THz pulse field strength, we observe that the intensity of the TFISH signal from the SiN detector is approximately 14–17 times larger than the signal from the SiO₂ detector. As has also been reported earlier,^[11] the SiN detector thus offers much better sensitivity and overall performance. The much higher applicable bias electrical field strength in the solid-state detector is particularly important, not only for the general signal strength and dynamic range of the detector but also for its linearity with respect to the THz field strength. As the peak THz electrical field strength at the focus of the air-plasma THz source can readily reach MVcm⁻¹ levels, the maximal bias electrical field allowed in air (30 kVcm⁻¹) is too small to modulate the high THz field efficiently. With the ABCD technique, significant attenuation of the incident THz wave can therefore be necessary to obtain linear waveform detection, which may compromise a good signal-to-noise level. In the case of the SSBCD device, due to the much higher dielectric breakdown strength (the maximum bias electrical field reached 212 kVcm⁻¹ in our detector before dielectric breakdown), attenuation of the incident THz wave is not as critical for efficient lock-in detection of the modulated TFISH signals.

A typically measured THz waveform with the SiN detector is shown in [Figure 5a](#) together with a background scan recorded with the THz beam blocked by a metal screen. The THz pulse energy measured at the detector was 0.62 μ J from a 1.4- μ m-driven two-color air-plasma, optical probe pulse energy was 140 nJ with a pulse duration of 40 fs, and the total bias voltage on the detector was 970 V. The peak dynamic range (DR) of the measured THz waveform is $>10^3$ (>60 dB power DR) as seen in the comparison of the spectral amplitude to the background in [Figure 5b](#). The detected spectra show an ultra-broadband detection bandwidth well exceeding 30 THz, which, to the best of our knowledge, is the broadest detection range reported so far with the SSBCD technique. As a side note, we could record a THz time trace even with sub-nJ (0.9 nJ) optical probe pulse energy (see [Supporting Information](#)) by pushing the bias voltage close to the dielectric breakdown limit (1060 V). This low probe energy is an order of magnitude lower than previously reported.^[11]

It is worth noting that both DR and signal-to-noise ratio (SNR) are crucial for accurately extracting THz frequency nonlinearity from ABCD and SSBCD measurements. In our experiments, ABCD and SSBCD were conducted under the same conditions, differing only in the active media used and the energy requirements of the probe pulses for the TFISH generation process. We observed no significant differences in SNR or DR between the two methods when optimally tuned. In the time domain the SNR reached approximately 87, while the DR reached 1748 (see [Supporting Information](#) for the detailed SNR and DR characterization). Waveform acquisition generally took 1–2 min at a laser repetition rate of 1 kHz. When employing slower waveform acquisition to increase signal averaging, DR improved substantially. However, SNR tended to decrease due to the slow drift in the output of the driving Ti:sapphire laser amplifier. These DR

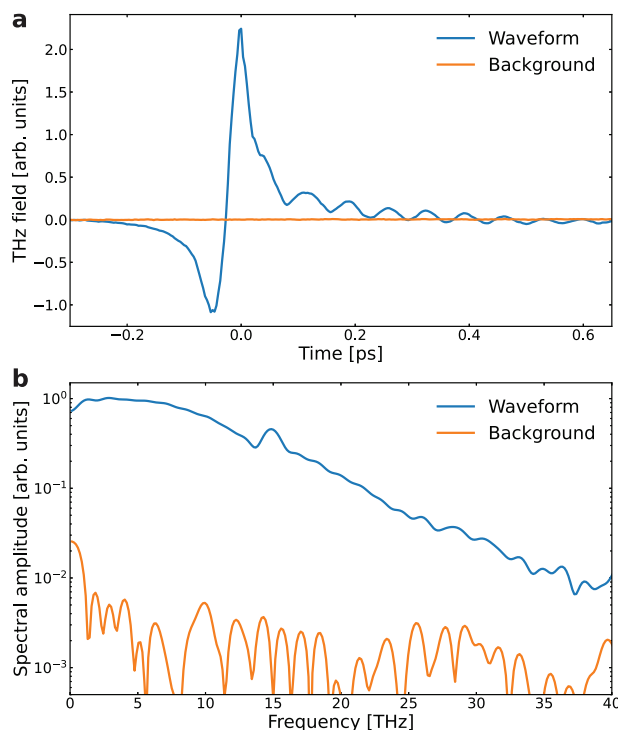


Figure 5. THz waveform measurement based on the SiN detector. a) Measured THz waveform signal and background measurement with blocked THz beam. b) Corresponding spectra indicate ultra-broadband detection and a peak dynamic range of $>10^3$.

and SNR characteristics are on par with those reported for kHz-repetition-rate laser amplifier-driven THz-TDS systems, whether they use ABCD,^[30] SSBCD,^[10,11] or EO-sampling detection. In systems utilizing quieter and MHz-repetition-rate fs oscillators, both SNR and DR can be enhanced further when operating under ideal conditions.^[31,32]

5. Measurement of $\chi^{(3)}(\Omega)$ Across the THz Frequency Range

[Figure 6a](#) shows three THz waveforms, which are proportional to the intensity of the generated TFISH signal near 400 nm, detected with different active materials for the TFISH in ABCD or SSBCD. The air detection (ABCD, blue curve) waveform is a rather smooth, asymmetric single-cycle pulse. Since air (essentially pure nitrogen in our experimental conditions) is dispersionless regarding its third-order nonlinearity in both the optical and THz frequency ranges, the THz spectra based on air detection can serve as a reference for the characterization of other nonlinear detection media. For the SiO₂-based SSBCD detector, a very pronounced ringing feature is observed in the detected time-domain trace (orange curve in [Figure 6a](#)), and prominent enhancements are observed in the spectrum of the detected signal, which indicates resonant enhancement of $\chi^{(3)}$ induced by the vibrational modes (see [Supporting Information](#) for data on linear SiO₂ spectroscopy). The frequencies of these enhancements are on the high side of the infrared absorption frequencies due to a combination of enhanced nonlinearity, increased absorption,

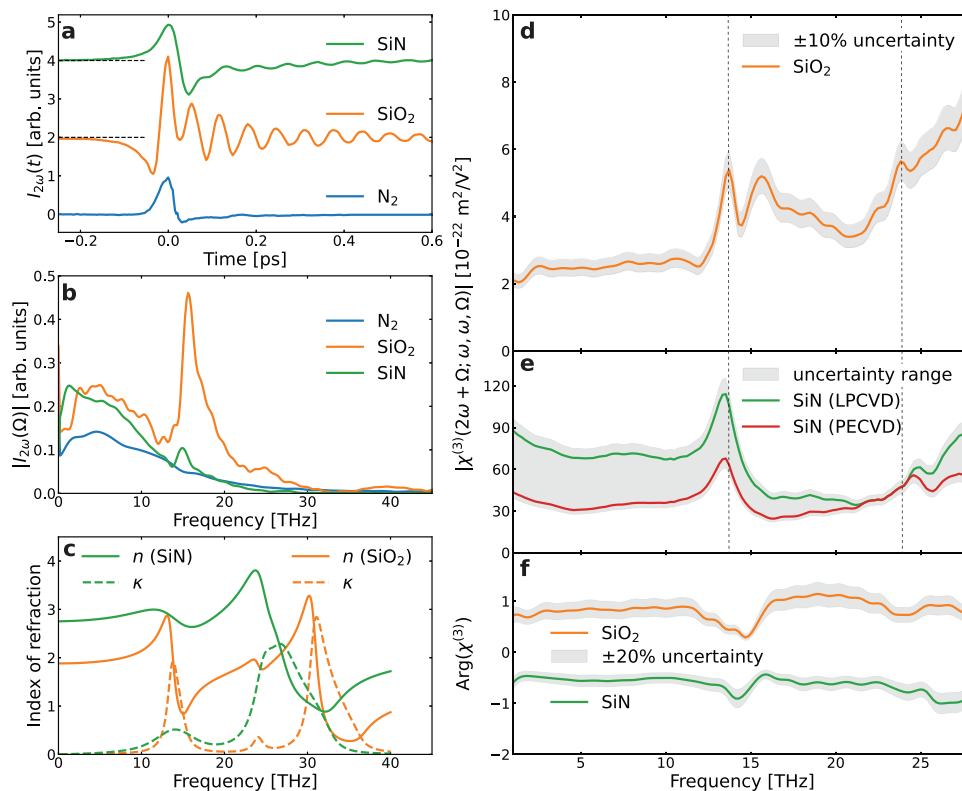


Figure 6. a) THz waveform detection from three active detecting materials: N_2 atmosphere (blue), SiO_2 (orange), and SiN (green). The THz source is the same for all detectors, but detector parameters vary between the scans. b) The spectra of the measured waveforms. Compared to the air-based detection, the SiO_2 -based detection shows spectral features near 13, 16, 25, and 40 THz (black dashed lines). c) real and imaginary parts of the parametrized Lorentz models of the refractive index of our SiO_2 thin film (own measurements, see [Supporting Information](#)) and SiN (Cataldo et al.^[33]). Measured $|\chi^{(3)}(2\omega + \Omega; \omega, \omega, \Omega)|$ as function of the THz frequency $\Omega/2\pi$ for d) SiO_2 and e) SiN (LPCVD, green and PECVD, red), with a probe wavelength of 800 nm ($\omega = 2\pi \cdot 375$ THz). Dashed lines guide the eye to show that resonance frequencies in SiO_2 are not identical to those nearby resonances in SiN . f) Phase of $\chi^{(3)}(2\omega + \Omega; \omega, \omega, \Omega)$ for SiO_2 and SiN . See main text for discussion of uncertainty intervals (gray, shaded areas).

and possibly phase matching in the vicinity of each resonance. Compared to the air-based detection, the SiO_2 -based detection thus shows enhancements near 16, 25, and 39 THz. For the SiN -based SSBCD detector, the known vibrational features in the relevant range are at 15 THz and 27–28 THz. The index of refraction and extinction coefficient of SiO_2 (own data, see [Supporting Information](#)) and SiN (Cataldo et al.^[33]) are shown in Figure 6c.

Based on the known detection parameters for each recorded time trace, we can use Equation (3) to calculate the absolute value of $\chi^{(3)}$ of silica across the bandwidth of the detected signals, and following this, Equation (4) is used to calculate the value of $\chi^{(3)}$ for SiN across the THz signal bandwidth. All the presented waveforms via either ABCD or SSBCD are directly detected THz waveforms without deconvolution of the 40-fs optical probe pulse. This deconvolution has no influence on the $\chi^{(3)}$ calculation since they are identical for ABCD and SSBCD, so they naturally cancel each other. This being said, this deconvolution effect essentially sets the upper frequency limit of the detected waveform, and thus of the $\chi^{(3)}$ determination.

Figure 6d shows $\chi^{(3)}(\Omega)$ for SiO_2 and Figure 6e shows $\chi^{(3)}$ for two variations of thin-film SiN (red and green curves), using identical focusing conditions and $L = (2000, 1, 0.5) \mu m$, $P = (1.2, 1.2, 0.19) mW$, $E_{bias} = (30, 120, 160) kVcm^{-1}$ for the N_2 , SiO_2

and SiN , measurements, respectively. The two variations of the SiN material correspond to the two known extremes of the refractive index in the visible and near-UV of thin-film SiN grown in our clean room (LPCVD = liquid-phase chemical vapor deposition, PECVD = physically enhanced chemical vapor deposition).^[34] As shown by Beliaev et al.,^[34] the refractive index in the visible and near-UV varies significantly with the fabrication method and the film thickness, which introduces the indicated uncertainty on the extracted nonlinearity due to the specific phase matching conditions. For each device, we have calculated the best estimate of the coherence length of the TFISH process for these two material variations ($\Delta k = k_{2\omega} - k_{\omega} - k_{\Omega}$, see [Supporting Information](#)), and for each THz frequency used the minimum value of the coherence length and physical film thickness as the effective interaction length. The transmission functions $t_{SiO_2}(\Omega)$ and $t_{SiN}(\Omega)$ are calculated in an FEM simulation where the frequency-dependent refraction and absorption of the materials, as well as field enhancement near the bias electrodes is taken into account. For details, see Supporting Information.

The gray band surrounding the SiO_2 data in Figure 6d indicates a conservative combined 10% uncertainty due to uncontrollable factors such as the limited precision of the SiO_2 film thickness.

We observe three features in the measured $\chi_{\text{SiO}_2}^{(3)}$, at 13.7, 15.7, and 23.8 THz. The measured $\chi_{\text{SiN}}^{(3)}$ displays an overall magnitude that depends on the composition due to the fabrication details (LPCVD or PECVD) chosen as the basis of the phase matching calculation, and we see spectral features at 13.4 and 24.7 THz. The overall nonlinearity is 10–15 times higher than for SiO₂. The dashed, vertical lines in Figure 6d,e shows that the spectral positions of the resonances in SiO₂ and SiN are close to each other but not identical.

The experimental peak magnitude of the $\chi_{\text{SiO}_2}^{(3)}$ within our range is $(5.3 \pm 0.5) \cdot 10^{-22} \text{ m}^2\text{V}^{-2}$, with an increasing trend toward the highest frequencies, possibly due to the 31-THz vibrational resonance that is just outside the useful data extraction range. The theoretical nonlinear susceptibility in the TFISH spectrum at resonance shown in Figure 2a is equal to $3 \cdot 10^{-22} \text{ m}^2\text{V}^{-2}$, which is in good qualitative agreement with the experimental values. On the other hand, away from the resonance, the theoretical model predicts orders-of-magnitude lower nonlinearity than observed in the experiment, where the variation of the magnitude of the nonlinearity is within a factor of three of the peak value.

We believe that this discrepancy is due to the fundamental simplification in the theoretical model that there are only a few active vibrational modes in the glass. This is not true in fused silica (or other amorphous materials). The Raman spectrum of crystalline SiO₂ (quartz) has a sharp resonance at 465 cm^{-1} (13.95 THz),^[35] whereas fused silica has a broad, low-frequency tail in its Raman spectrum below the 465-cm^{-1} line.^[36] This low-frequency tail to the Raman activity is also seen in the Raman gain spectrum of fused silica fibers.^[37,38]

The additional low-frequency contributions to Raman processes in amorphous SiO₂ can be attributed to a significant disorder-induced vibrational density of states^[39] that spans the entire 1–25 THz range. Inspecting Equation (7), we see that the nonlinearity is proportional to the number density of the vibrational modes N . Hence, as a rough first estimate, introducing a vibrational density of states instead of three distinct resonances, it can be expected that such a model for $\chi^{(3)}$ will be much closer to the experimentally determined TFISH $\chi^{(3)}$. Further theoretical development in this direction is beyond the scope here, but will certainly be valuable for a deeper understanding of the THz-induced nonlinearities of amorphous materials.

6. Benchmarking of SSBCD Device Performance in Quantitative Spectroscopy

GaAs is one of the most studied semiconductors. It is a direct bandgap semiconductor with a zincblende crystal structure, and a bandgap of 1.42 eV. Due to the simple crystal structure, the phonon spectrum of GaAs is at first glance rather simple, with a transverse optical (TO) phonon in the far infrared as the strongest feature. Hence, in its undoped form, the dielectric properties of GaAs are determined by the TO phonon. To benchmark the capabilities of THz air photonics with the SSBCD device in spectroscopy we first performed a reflection measurement at normal incidence and at room temperature on a high-resistivity GaAs wafer with our standard ABCD setup, and then a transmission measurement of the same sample using the SSBCD device for

detection of the THz field. For the reflection measurements, we evaporated a 200-nm gold film on half of the wafer as a reference reflection area. The wafer was then translated perpendicular to the incoming beam between measurements. Measurements were performed with a temporal step size of 3.33 fs over a time window of 10 ps. The details concerning the extraction of the permittivity from the time-domain data are given in the Supporting Information.

The permittivity as determined with the reflectivity measurements is shown in Figure 7a. The real and imaginary parts of the permittivity are shown as blue and orange curves, respectively. The light-colored bands indicate the standard deviation of the calculated permittivity, based on error propagation through the underlying equations. The inset to the right in Figure 7a shows the region close to the TO phonon.

The black, dashed curves in Figure 7a represent a fit of the Lorentz oscillator model to the experimental data, $\epsilon(\Omega) = \epsilon_\infty + A/(\Omega_{\text{TO}}^2 - \Omega^2 - i\Omega\Gamma)$, where Ω_{TO} is the resonance frequency, Γ is the damping rate, and A is the oscillator strength. The best-fit parameters are $\epsilon_\infty = 10.99 \pm 0.08$, $A = (4897 \pm 32) \text{ ps}^{-2}$, $\Omega_0 = (50.607 \pm 0.002) \text{ ps}^{-1}$, $\Gamma = (0.471 \pm 0.004) \text{ ps}^{-1}$.

The uncertainties indicate the 95% confidence intervals of the fit. The oscillator strength is related to the overall change of the real part of the permittivity across the resonance, $\Delta\epsilon = A/\Omega_{\text{TO}}^2 = 1.912 \pm 0.012$. The LO frequency can be estimated via $A = \epsilon_\infty(\Omega_{\text{LO}}^2 - \Omega_{\text{TO}}^2)$ so that $\Omega_{\text{LO}} = 54.83 \text{ ps}^{-1}$ (8.727 THz).

The damping rate corresponds to a decay time $\tau = 1/\Gamma = 2.12 \text{ ps}$. The remarkably good fit to the experimental data indicates that the TO phonon in GaAs is well described by the Lorentz model, and we are not able to determine any systematic deviations from this simple, classical model. However, the good agreement between model and experimental data does not necessarily settle the best value of the oscillator parameters. For instance, our value of the damping rate is lower than that measured by CARS spectroscopy, where a room-temperature value of $\Gamma = (0.703 \pm 0.132) \text{ ps}^{-1}$ was reported.^[42] The lower damping rate we observe follows the trend from earlier THz-TDS measurements.^[43] However, we do not observe a deviation from the Lorentzian shape of the resonance as reported in ref. [43].

We then used the same high-resistivity GaAs wafer (640 μm thickness) to benchmark the practical performance of the developed solid-state THz detector for spectroscopy against the reflection measurement. We implemented the SiN-based SSBCD device in our transmission-mode air-plasma-based THz-TDS system, with the extracted permittivity (real and imaginary parts) shown in Figure 7b. Details on the data set (time traces, spectra of the signals) are shown in the Supporting Information. black, dashed curves represent the same fit as shown in Figure 7a. The overall agreement between the fit with the measurement, especially with the real part of the measured permittivity, is convincing.

The very good agreement shows the capability of the SSBCD device in terms of signal-to-noise ratio and, importantly, linearity for quantitative spectroscopy across the 1–20 THz region. Interestingly, the transmission measurement deviates systematically from the Lorentz fit from the reflection measurement and reveals very weak but significant dispersive features in the imaginary part of the measured permittivity (orange data points in Figure 7b) both below and above the fundamental TO phonon

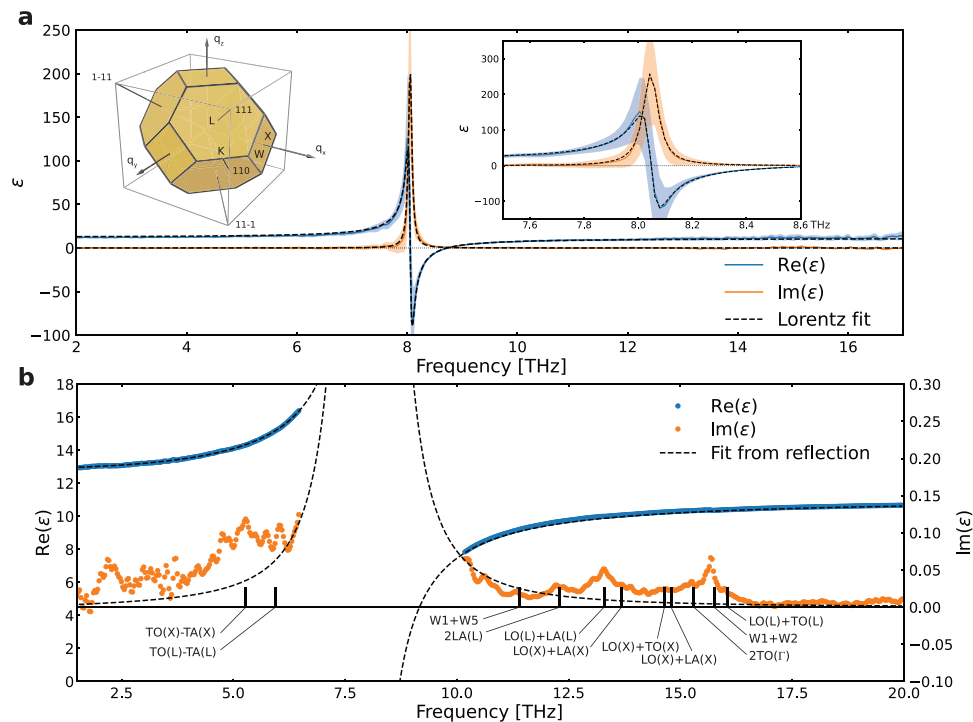


Figure 7. Permittivity of GaAs, measured a) in reflection geometry with ABCD. Solid curves (blue, orange) show the measurement, dashed curves show a Lorentz fit, and shaded areas indicate the 95% confidence interval of the fit. The Inset zooms onto the frequency region near the TO phonon resonance. b) Permittivity measured in transmission geometry with SSBCD. Blue and orange symbols show the measured data and the dashed curves show the same Lorentz fit as in (a). Vertical lines indicate known phonon combination band frequencies^[40,41] related to the symmetry points (L, X, W, T) indicated in the Brillouin zone illustration inset of (a).

band that are not visible in a reflection measurement. These features are known phonon combination bands,^[40,41] as indicated in the figure with the notation used by Abdullah et al. The most prominent combination band observed here are the W1+W2, LO(L,X)+LA(L,X), 2LA(L) bands, with indications of several other bands contributing to the background absorption in the 10–17 THz range. The Brillouin zone with the relevant symmetry points is shown as inset in Figure 7a.

7. Conclusion

In summary, we have shown a novel method for the quantitative determination of THz-frequency dispersion of the third-order nonlinearity $\chi^{(3)}(\omega, \omega, \omega, \Omega)$ of thin films of amorphous SiO₂ and SiN in the $\Omega/2\pi = 1 - 28$ THz frequency range, based on a calibrated comparison of detected THz signals from ABCD and detection in solid-state devices based on the two materials. We show that the vibrational modes in SiO₂ and silicon nitride in the THz range lead to the strong resonant enhancement and dispersion on nonlinearity, indicating promising nonlinear phenomena by utilizing the high $\chi^{(3)}$ for a variety of nonlinear optical investigations on the resonance frequencies. The method is generally applicable to other dielectrics and thus represents a significant advance of the characterization toolbox available for the development of new THz-frequency technology. The solid-state detectors implemented here use a modified electrode structure for distribution of the bias field, resulting in significantly enhanced detection bandwidth to above 40

THz and record-low requirements on the probe pulse energy that was pushed to the sub-nJ level. We have shown that solid-state detectors are capable of quantitative, nontrivial spectroscopy by comparing a reflection-based measurement of GaAs using ABCD with a transmission-based experiment of the same material using a solid-state detector, and found quantitative agreement across the available, extended frequency range. We believe that these developments will be beneficial for advanced pulse detection concepts, as well as static, pump-probe, and nonlinear multidimensional spectroscopy.

Supporting Information

Supporting Information is available from the Wiley Online Library or from the author.

Acknowledgements

The authors acknowledged Kjeld Dalgaard for the design and production of PCB boards, Huaqing Qiu for assistance with the delicate wire bonding of the SSBCD devices, and Jie Ji for assistance with gold deposition on GaAs. The authors acknowledged partial financial support from the Velux Foundation (00023215) and Independent Research Fund Denmark (ULTRA-TED: 9040-00360B and THz-GRIP: 2035-00265B). K. D. acknowledged Natural Sciences and Engineering Research Council of Canada's (NSERC) Discovery program (grant number RGPIN-2020-03989). The work at the University of Ottawa was also funded by the Canada Research Chairs Program and by the Natural Sciences and Engineering Research Council of Canada.

Conflict of Interest

The authors declare no conflict of interest.

Data Availability Statement

The data that support the findings of this study are available from the corresponding author upon reasonable request.

Keywords

nonlinear optics, terahertz detection, terahertz optics, ultrafast optics

Received: December 14, 2023

Revised: May 29, 2024

Published online:

- [1] J. Dai, X. Xie, X. C. Zhang, *Phys. Rev. Lett.* **2006**, *97*, 103903.
- [2] N. Karpowicz, J. M. Dai, X. F. Lu, Y. Q. Chen, M. Yamaguchi, H. W. Zhao, X. C. Zhang, L. L. Zhang, C. L. Zhang, M. Price-Gallagher, C. Fletcher, O. Mamer, A. Lesimple, K. Johnson, *Appl. Phys. Lett.* **2008**, *92*, 011131.
- [3] D. J. Cook, R. M. Hochstrasser, *Opt. Lett.* **2000**, *25*, 1210.
- [4] M. Kress, T. Löffler, S. Eden, M. Thomson, H. G. Roskos, *Opt. Lett.* **2004**, *29*, 1120.
- [5] X. Xie, J. M. Dai, X. C. Zhang, *Phys. Rev. Lett.* **2006**, *96*, 075005.
- [6] T. Wang, P. Klarskov, P. U. Jepsen, *IEEE Trans. Terahertz Sci. Technol.* **2014**, *4*, 425.
- [7] A. T. Tarekegne, B. Zhou, K. Kaltenecker, K. Iwaszczuk, S. Clark, P. U. Jepsen, *Opt. Express* **2019**, *27*, 3618.
- [8] D. G. Cooke, F. C. Krebs, P. U. Jepsen, *Phys. Rev. Lett.* **2012**, *108*, 056603.
- [9] M. R. Otto, L. P. R. de Cotret, D. A. Valverde-Chavez, K. L. Tiwari, N. Emond, M. Chaker, D. G. Cooke, B. J. Siwick, *Proc. Natl. Acad. Sci. USA* **2019**, *116*, 450.
- [10] A. Tomasino, A. Mazhorova, M. Clerici, M. Peccianti, S.-P. Ho, Y. Jestin, A. Pasquazi, A. Markov, X. Jin, R. Piccoli, S. Delprat, M. Chaker, A. Busacca, J. Ali, L. Razzari, R. Morandotti, *Optica* **2017**, *4*, 1358.
- [11] A. Tomasino, R. Piccoli, Y. Jestin, S. Delprat, M. Chaker, M. Peccianti, M. Clerici, A. Busacca, L. Razzari, R. Morandotti, *APL Photonics* **2018**, *3*, 8.
- [12] K. Dolgaleva, D. V. Materikina, R. W. Boyd, S. A. Kozlov, *Phys. Rev. A* **2015**, *92*, 2.
- [13] A. Tcytkin, M. Zhukova, M. Melnik, I. Vorontsova, M. Kulya, S. Putilin, S. Kozlov, S. Choudhary, R. W. Boyd, *Phys. Rev. Appl.* **2021**, *15*, 054009.
- [14] S. Zibod, P. Rasekh, M. Yildirim, W. Cui, R. Bhardwaj, J.-M. Ménard, R. W. Boyd, K. Dolgaleva, *Adv. Opt. Mater.* **2023**, *11*, 2202343.
- [15] M. C. Hoffmann, N. C. Brandt, H. Y. Hwang, K. L. Yeh, K. A. Nelson, *Appl. Phys. Lett.* **2009**, *95*, 231105.
- [16] M. Zalkovskij, A. C. Strikwerda, K. Iwaszczuk, A. Popescu, D. Savastru, R. Malureanu, A. V. Lavrinenko, P. U. Jepsen, *Appl. Phys. Lett.* **2013**, *103*, 221102.
- [17] T. Kampfath, R. K. Campen, M. Wolf, M. Sajadi, *J. Phys. Chem. Lett.* **2018**, *9*, 1279.
- [18] T. Brabec, C. Spielmann, P. F. Curley, F. Krausz, *Opt. Lett.* **1992**, *17*, 1292.
- [19] X.-C. Zhang, J. Xu, *Introduction to THz wave photonics*, Springer, Berlin, Heidelberg **2010**.
- [20] V. Mizrahi, D. P. Shelton, *Phys. Rev. Lett.* **1985**, *55*, 696.
- [21] P. Sitz, R. Yaris, *J. Chem. Phys.* **1968**, *49*, 3546.
- [22] D. J. Cook, J. X. Chen, E. A. Morlino, R. M. Hochstrasser, *Chem. Phys. Lett.* **1999**, *309*, 221.
- [23] T. Suter, A. Tomasino, M. Savoini, S. Houver, R. Morandotti, S. L. Johnson, E. Abreu, *Opt. Express* **2022**, *30*, 45202.
- [24] R. W. Boyd, *Nonlinear Optics*, 4th edition, Academic Press, Elsevier, Amsterdam **2020**.
- [25] M. Clerici, M. Peccianti, B. E. Schmidt, L. Caspani, M. Shalaby, M. Giguère, A. Lotti, A. Couairon, F. Légaré, T. Ozaki, D. Faccio, R. Morandotti, *Phys. Rev. Lett.* **2013**, *110*, 253901.
- [26] A. Nguyen, K. J. Kaltenecker, J. C. Delagnes, B. Zhou, E. Cormier, N. Fedorov, R. Bouillaud, D. Descamps, I. Thiele, S. Skupin, P. U. Jepsen, L. Bergé, *Opt. Lett.* **2019**, *44*, 1488.
- [27] T. Wang, K. Iwaszczuk, E. A. Wisberg, E. V. Denning, P. U. Jepsen, *J. Infrared, Millimeter, Terahertz Waves* **2016**, *37*, 592.
- [28] P. U. Jepsen, D. G. Cooke, M. Koch, *Laser Photonics Rev.* **2011**, *5*, 124.
- [29] P. U. Jepsen, *J. Infrared, Millimeter, Terahertz Waves* **2019**, *40*, 395.
- [30] X. Lu, X.-C. Zhang, *Appl. Phys. Lett.* **2011**, *98*, 151111.
- [31] M. Naftaly, R. Dudley, *Opt. Lett.* **2009**, *34*, 1213.
- [32] M. Koch, D. M. Mittleman, J. Ornik, E. Castro-Camus, *Nat. Rev. Methods Primers* **2023**, *3*, 48.
- [33] G. Cataldo, J. A. Beall, H.-M. Cho, B. McAndrew, M. D. Niemack, E. J. Wollack, *Opt. Lett.* **2012**, *37*, 4200.
- [34] L. Y. Beliaev, E. Shkondin, A. V. Lavrinenko, O. Takayama, *Thin Solid Films* **2022**, *763*, 139568.
- [35] K. J. Kingma, R. J. Hemley, *Am. Mineral.* **1994**, *79*, 269.
- [36] G. Winterling, *Phys. Rev. B* **1975**, *12*, 2432.
- [37] R. H. Stolen, E. P. Ippen, *Appl. Phys. Lett.* **1972**, *22*, 276.
- [38] D. J. Dougherty, F. X. Kärtner, H. A. Haus, E. P. Ippen, *Opt. Lett.* **1995**, *20*, 31.
- [39] S. N. Taraskin, S. R. Elliott, *Phys. Rev. B* **1997**, *56*, 8605.
- [40] A. K. W. Abdullah, Ph.D. Thesis, Faculty of Science, Royal Holloway and Bedford New College, University of London, **1986**.
- [41] A. K. W. Abdullah, T. J. Parker, *Mikrochimica Acta* **1988**, *2*, 361.
- [42] F. Ganikhanov, F. Vallée, *Phys. Rev. B* **1997**, *55*, 15614.
- [43] G. C. Cho, P. Y. Han, X. C. Zhang, H. J. Bakker, *Opt. Lett.* **2000**, *25*, 1609.